Hydrodynamics of the Mixing Head in RIM: LDA Flow-Field Characterization

André M. Teixeira
Sun Chemical Portugal, Serzedo, Portugal

Ricardo J. Santos, Mário Rui P. F. N. Costa, and José Carlos B. Lopes
Laboratory of Separation and Reaction Engineering, Chemical Engineering Department, Faculdade de Engenharia da Universidade do Porto, 4200-465 Porto, Portugal

DOI 10.1002/aic.10454
Published online April 27, 2005 in Wiley InterScience (www.interscience.wiley.com).

The flow field in a reaction injection molding (RIM) machine mixing head was characterized using the laser Doppler anemometry (LDA) technique. This study covered the range of Reynolds numbers from 50 to 600, normally used in industry for the RIM process. The three time-averaged spatial distributions of velocity components, inside the mixing head, were obtained: the two horizontal components directly from LDA measurements and the third component through numerical integration. Flow-field distributions were also computed, including probability density functions of the velocity, turbulence intensity, and Reynolds stresses. The present study provides new insights into the mixing mechanisms involved in RIM machines and more generally in opposed-jet mixers. In particular, new features were found: the dominant role of interactions of the opposed jets as the main mixing mechanism; and that the flow-field dynamics evolve with Re at constant Strouhal number within the typical range, 150 ≤ Re ≤ 600, of operation of RIM machines. © 2005 American Institute of Chemical Engineers *AIChE J,* 51: 1608–1619, 2005
Keywords: RIM, impinging jets, mixing, fluid mechanics, reactor analysis

Introduction

The injection molding process with chemical reaction, usually referred as *reaction injection molding* (RIM), is used in the production of plastic components with complex geometries, starting from low-viscosity monomers or oligomers. The process consists mainly in a very intense contact of two or more reacting viscous liquids in a small mixing head, flowing afterward to a larger mold where most polymerization takes place. This process is implemented in high-pressure RIM machines that are designed for the simultaneous injection in the mixing head of reactants at stoichiometric rates and at very high velocities, to achieve the necessary degree of homogenization and reaction.[1] The quality of mixing is of primary importance to achieve a high degree of polymerization and, in this way, a plastic with the necessary mechanical properties.[2-4] Thus, it is nowadays a well-accepted idea that the contact stage of the reactants in the mixing head constitutes the heart of the process. The major limitation, on obtaining the desired mixing quality in the mixing head, is the very fast kinetics of the initial stages of polymerizing reaction usually associated with this process.[5]

Typical mixing heads used in these machines are small cylindrical chambers, with characteristic diameters of the order of 10 mm, with two lateral surface nozzles, generally orienting both jets to impinge axially on each other, generating an intensive mixing upon impact of the jets. Usually the opposed jets enter the mixing head with velocities within the range of 10 to 100 m/s and stop over very short distances, of the order of a half-diameter of the mixing head, creating substantial liquid

Correspondence concerning this article should be addressed to J. C. B. Lopes at lopes@fe.up.pt.

decelerations—a very strong source for mechanical instabilities—that intensively promote the mixing mechanisms. In spite of the strong dynamics involved in this flow field, completely developed turbulent flow cannot be observed, given the high viscosity (up to 1 Pa·s) of the reactants. Typical operating Reynolds numbers, based on nozzle diameter, are in the range of 100 to 500. For the injection of these highly viscous liquid reactants in the mixing head, at the required velocities through the lateral nozzles with diameters ranging from 1 to 3 mm, the use of strong positive displacement pumps, capable of reaching high injecting pressures up to 10 MPa, is required.[6]

The industrial importance of polymers manufactured using RIM and the effect of mixing on their final mechanical properties have been the driving force for many studies on this particular subject. Three different main research approaches to the problem have been followed:

(1) The first, through experiments designed to obtain data on a single measurable physical characteristic of the process, that can be directly or indirectly associated with the efficiency of mixing. This approach mainly provides an assessment of the effectiveness of mixing under different operating conditions and design parameters, although it never directly unveiled the mixing mechanisms. The experimental characteristics that have been measured for mixing assessment are:

- change of a tracer concentration at the outlet[7,8] or inside the mixing head[9]
- striation thickness distributions in the final mold piece obtained from the introduction of a dye in one of the reactants[2,10]
- the adiabatic temperature rise from polymerization at the mold that, because of the exothermic nature of the reaction, increases with higher conversion of the reactant[2,5,10,11]
- the distribution of products of test reactions for quantification of micromixing [12-14]
- the morphology of the final polymer product[3,15]

(2) The second approach, which focuses on the experimental hydrodynamic characterization of the flow field. Here can be included the simple observation studies of the flow in the RIM mixing head,[8-10,16,17] which made possible the qualitative characterization of the flow patterns, up to the more detailed quantitative characterizations of the flow-field studies. These include the measurement of oscillating frequencies in the velocity field[18-21] and the evaluation of flow-field velocity maps[16,19-24] based on several sophisticated anemometry laser techniques such as particle image velocimetry (PIV), particle tracking velocimetry (PTV), and laser Doppler anemometry (LDA) measurements.

(3) Finally, the approach based on the development of theoretical models that aim to predict the degree of mixing from the operating parameters of the RIM machine.[10,13,25]

For the characterization of mixing in the RIM process there are some common features in the literature on this subject. The existence of a critical Reynolds number, above which the degree of mixing is maximum and practically invariant for higher Reynolds values, is an important observation present in all studies of the Reynolds number effect.[2,5,8,10-13,18,21] However, the mechanisms underlying this critical value are still unclear. The conclusion of Sebastian and Boukobbal[5] is also worthy of note: the degree of mixing for a certain Reynolds number at some determined operational conditions can often be improved by changing the mixing head geometry. Finally, several studies have reported the existence of typical frequencies for fluid velocity oscillations.[18-20] Further experimental evidence of those typical frequencies are discussed in this paper.

The multiple factors involved in this process—such as the geometry of the mixing head, the hydrodynamic features of high viscosity liquids, and momentum ratios of opposing jets, coupled with simultaneous mass transfer and chemical reaction between the two jet streams—are key restrictive issues for the complete understanding of the mixing mechanisms in RIM. Despite the significant contributions of the works previously referenced, there is not yet enough insight into the flow field to establish consolidated relationships between the operational conditions and the mixing efficiency. This has been the main driving force behind this study. In the following sections experimental data obtained from the LDA measurements in the mixing head of a pilot RIM machine will be presented, with special focus on the study of the dependency of the flow characteristics with the Reynolds number.

Experimental

Setup

The experimental work was performed in a pilot RIM machine, shown in Figure 1, equipped with a mixing head, shown in Figure 2, with typical dimensions used in industry of 10 mm diameter ($\pm$0.05 mm) and 50 mm height. The two injectors were precisely aligned horizontally and located at a distance of 5 mm from the top of the mixing head. This particular placement was chosen to ensure maximum strength of the jets at the impingement point, by reducing curving effects resulting from top wall friction and allowing the formation of a toroidal vortex at the top of the mixing head, as will be shown later. Each injector is made of a tube with a calibrated diameter of 1.496 $\pm$ 0.001 mm and length of 50 mm, long enough to ensure fully developed Poiseuille flow at the injectors' outlet. To ensure the precise alignment of the injector axis ($\pm$0.005 mm), the injectors were placed in a solid steel block where the mixing head was drilled by electroerosion. The mixing head's top is a fused silica optical window.

Other details of the RIM machine can be found in Figure 1 and the detailed drawing of the mixing head and the coupled discharge mould are found in Figure 2. In particular Figure 2 shows the Cartesian frame of reference used throughout this paper, where the x-direction is chosen coincident with alignment of the injectors, the z-direction is the vertical mixing head axis, and the y-axis is normal to the x–z vertical plane. The frame origin is at the top point of the vertical axis.

The flow diagram of the pilot RIM machine is also shown in Figure 1. For the experiments, the fluids were pumped from the tanks to the injectors by two positive-displacement gear pumps. The flow rates were controlled accurately ($\pm$2%) by computer. The flow rates were set a priori from a calibration curve, and computer feedback control was implemented by monitoring in real time the rate of change of level in the tanks with hydrostatic differential pressure transducers coupled to both feed tanks. The fluids used in the experiments were two aqueous solutions of glycerol with different viscosities: Sol. 1 with 80% (w/w) and Sol. 2 with 72.3% (w/w) concentration of glycerol. The relevant physical properties of these glycerol solutions at the experimental temperature of 20°C are shown in Table 1.

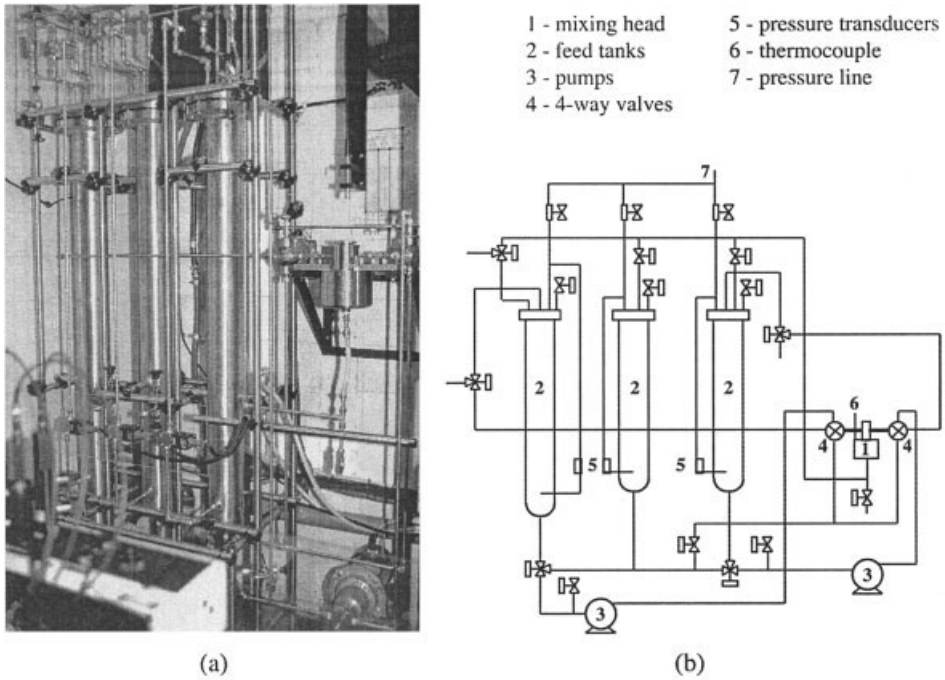

Figure 1. Pilot RIM machine: (a) photo of experimental setup; (b) flow diagram.

The use of two viscosity fluids increased the hydrodynamic range for experiments, and allowed the testing of the *similarity principle* in the RIM mixing process.

The velocity measurements were performed with LDA equipment from TSI® by Teixeira,[26] for the simultaneous measurement of two orthogonal-velocity components that in the particular arrangement for these experiments corresponded only to the two horizontal components of the velocity vector inside the mixing head. The laser source is a 5-W argon-ion tube and its beam is split into two monochromatic beams, with different colors for each velocity component measurement, forming two independent measuring channels (channel 1: green, $\lambda = 514.5$ nm; channel 2: blue, $\lambda = 488.0$ nm). The LDA system was operated in backscatter mode, and to avoid the inherent Doppler ambiguity on the determination of velocity direction, beam-frequency shift was used. For the experiments at the lower velocity range, up to 5 m/s, the imposed shift was 5 MHz, and the backscattered signal was band-pass filtered in the range from 1 to 10 MHz. For higher velocities, the applied band-pass filter was in the range 3 to 20 MHz and the frequency shift was 10 MHz. The fluids were seeded with neutrally buoyant nylon particles with diameter 4.0 ± 1.5 μm. All the characteristics of the laser beam and measuring volume are shown in Table 2 for both channels. The measuring point of the LDA probe was accurately positioned (± 0.025 mm) within the mixing head through the optical window, with a computer-controlled three-axis robot.

Conditions

The Reynolds number for the mixing head of a RIM machine is based on the diameter of the injectors, and defined as[7]

$$\mathrm{Re} = \frac{\rho v_{inj} d}{\mu} \tag{1}$$

where v_{inj} is the superficial velocity at the injectors; d is the diameter of injectors; and ρ and μ are the density and viscosity of the fluid, respectively. Experiments were performed in the hydrodynamic range of $50 \leq \mathrm{Re} \leq 600$, corresponding to varying the injectors superficial velocities in the range of $1.66 \leq v_{inj} \leq 10.9$ m/s with corresponding mixing head passage time maximum of 670 ms and minimum of 102 ms. The experimental parameters are summarized in Table 3.

With the purpose of performing a detailed scanning of the mixing head hydrodynamic field, two different spatial measurement grids were defined as shown in Figure 3. The first grid, Grid 1, with a larger number of points (1637) was used for a more detailed characterization of the flow field at Re = 100, 300, and 500, and Grid 2 with 51 points was used for Re = 50, 100, 150, 200, 300, 330, 400, 500, and 600. Grid 1 has 29 horizontal planes, and in each plane the points are equally spaced with $\Delta x = \Delta y = 1$ mm. Grid 2 has only three horizontal planes, at $z = 2.5$, 5, and 10 mm, with nine points in each plane. The observed typical data rates for LDA measurements ranged from a maximum of 4000 Hz on the planes near the jets, to a minimum of 20 Hz at the outlet.

Experimental Data

At the onset of the analysis of the LDA experimental data, it should be pointed out that in spite of the fact that all the experiments were performed at steady-state injection conditions, only with the experiment at Re = 50 was a laminar steady state observed. In all the other experiments, a strong

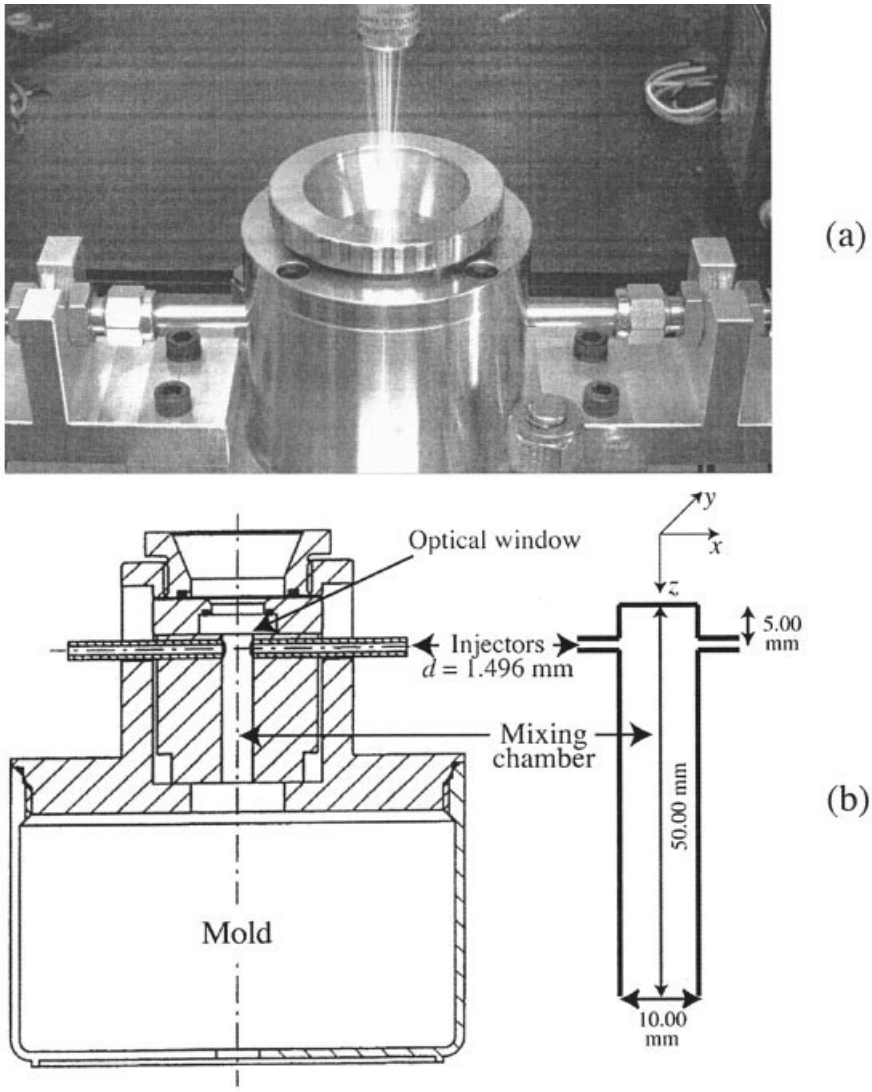

Figure 2. (a) Top view of mixing head with LDA probe and (b) detailed design and dimensions.

variation of the local velocities with time was observed, but their statistical time averages were found rapidly converging to steady values. Therefore, the velocity field will be statistically analyzed in terms of mean velocity values, velocity distribution functions, turbulence intensities, Reynolds stresses, and velocity spectral analysis. The main objective was to investigate the existence of possible flow structures such as flow symmetry, vortices, and recirculation patterns that would elucidate the nature of mixing mechanisms and the local characterization of turbulence in terms of intensity and anisotropy. This is the usual strategy for the study of turbulent flows, but in this particular case special care should be taken because the range of Reynolds number values, $50 \leq Re \leq 600$, is so low that *real turbulent flow* is not expected, that is, locally and instantaneously the flow is laminar in some sense. The fact is, as will be shown later, that a very strong *dynamic chaotic flow* is established at these low values of Re, as observed by Macosko

Table 1. Physical Properties of the Aqueous Glycerine Solutions

Fluid	Property	Value
Sol. 1	Refractive index	1.4430
(80.0% w/w)	Density (kg/m^3)	1207
	Viscosity (Pa · s)	0.0600
Sol. 2	Refractive index	1.4315
(72.3% w/w)	Density (kg/m^3)	1187
	Viscosity (Pa · s)	0.0286

Table 2. Characteristics of the Laser Beams and Measuring Volumes

Parameter	Channel 1 Green	Channel 2 Blue
Wavelength	514.5 nm	488.0 nm
Half interception angle (Sol. 1)	2.64°	2.64°
Half interception angle (Sol. 2)	2.66°	2.66°
Measuring volume diameter	0.11 mm	0.11 mm
Measuring volume length	2.4 mm	2.3 mm
Number of fringes	20	21
Fringe spacing (Sol. 1)	5.58 μm	5.29 μm
Fringe spacing (Sol. 2)	5.53 μm	5.25 μm

Table 3. Experimental Flow Conditions

Experiment	Re	Grid Type	Fluid (See Table 1)	v_{inj} (m/s)	q_{inj} (m^3/s)	Mixing Head Passage Time (s)
1	100	1	Sol. 1	3.31	5.86×10^{-6}	0.335
2	300	1	Sol. 1	9.94	1.76×10^{-5}	0.112
3	500	1	Sol. 2	8.03	1.42×10^{-5}	0.138
4	50	2	Sol. 1	1.66	2.93×10^{-6}	0.670
5	100	2	Sol. 1	3.31	5.86×10^{-6}	0.335
6	150	2	Sol. 1	4.97	8.78×10^{-6}	0.223
7	200	2	Sol. 1	6.63	1.17×10^{-5}	0.167
8	200	2	Sol. 2	3.21	5.68×10^{-6}	0.346
9	300	2	Sol. 1	9.94	1.76×10^{-5}	0.112
10	300	2	Sol. 2	4.82	8.51×10^{-6}	0.230
11	330	2	Sol. 1	10.9	1.93×10^{-5}	0.102
12	400	2	Sol. 2	6.42	1.14×10^{-5}	0.172
13	500	2	Sol. 2	8.03	1.42×10^{-5}	0.138
14	600	2	Sol. 2	9.64	1.70×10^{-5}	0.115

and coworkers,[2] that effectively promotes the mixing of very viscous liquids within the RIM mixing head.

Mean velocities

The dimensionless velocities (v^*) are normalized by the average spatial velocity at the injectors (v_{inj}) as

$$v^* = \frac{v}{v_{inj}} \tag{2}$$

and the unbiased time-averaged velocities ($\bar{v}^*$) at every position are calculated by

$$\bar{v}^* = \frac{\sum_{i=1}^{n_t} v(i) t_{s_i}}{(\sum_{i=1}^{n_t} t_{s_i}) \times v_{inj}} \tag{3}$$

where n_t is the total number of data sample points and t_{s_i} is the sample time interval duration of the ith sampling. All the reported averages are based on a minimum of $n_t = 2000$ at the outlet region, up to $n_t = 10{,}000$ on the planes near the jets.

From the direct simultaneous measurement of the two horizontal components, v_x^* and v_y^*, the horizontal velocity vector can be computed. Figure 4 shows the time-averaged horizontal velocity vectors maps for the measured planes at $z = 1$, 3, 5, 10, 20, and 50 mm for experiments 1, 2, and 3 (Re = 100, 300, and 500).

In all vector maps of Figure 4 a rather remarkable and consistent symmetry relative to the x–z and y–z vertical planes is found. The y–z symmetry is consistent with the fact that both injectors are feeding equal flow rates, and the x–z symmetry reveals that, in spite of the observed very strong dynamic chaotic behavior of the local velocities, the time-averaged flow

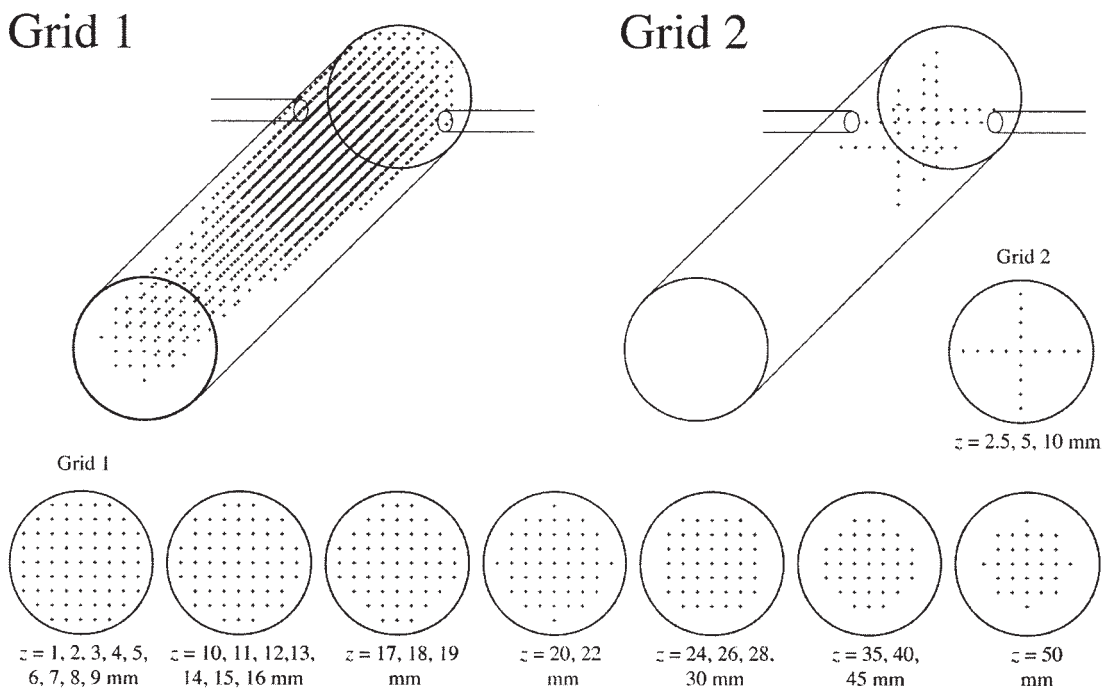

Figure 3. Spatial distribution of the measuring points for Grid 1 and Grid 2.

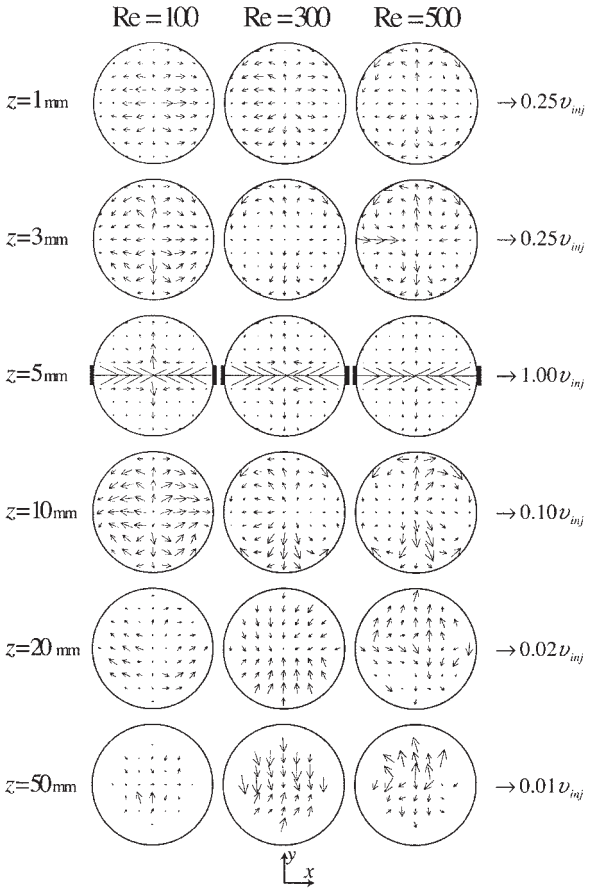

Figure 4. Vector maps for horizontal velocity components for experiments 1, 2, and 3 at horizontal planes: z = 1, 3, 5, 10, 20, and 50 mm.

field still maintains the balance feature imposed by the symmetry of the injections.

The vector map at the axis of the injectors, $z = 5$ mm, that contains the *impingement point* at $x = 0$, $y = 0$, and $z = 5$ mm, shows that the jets from the injectors lose neither their momentum nor their integrity at this region. Thus the average velocity in the region in front of the injectors maintains the average exit velocity (notice the vector scale on the right of Figure 4), but only at the impingement point does the average horizontal velocity fall drastically to zero. In addition, a relatively weak horizontal recirculation pattern is observed. Furthermore, this plane divides the flow field into two very distinctive regions: (1) a plain *recirculation zone* at the top and (2) a predominantly *convection zone* from the injectors toward the exit of the mixing heads.

At the top recirculation zone all the vector maps obtained from experiments show a strong horizontal motion, where the average horizontal velocities are of the order of 1/10 of v_{inj}, and their vertical distributions clearly show (Figure 4) the formation of a toroidal vortex placed at the top of the mixing head.

At the convective zone below the injectors, the flow is mainly vertical toward the exit of the mixing head, and the horizontal motion decreases rapidly with the distance from the injectors. This decrease is more intense in the core regions, indicating a preferential downward-vertical motion through the center of the mixing head. Nevertheless, some well-organized pattern of horizontal velocities was observed, indicating the possibility of an upward-vertical recirculation motion (that is, effective back-mixing) that would simultaneously promote convective mixing with the global convective motion toward the exit.

To explore this back-mixing possibility, actual knowledge of the vertical velocity v_z is necessary. Because this could not be obtained directly from these LDA measurements, an alternative estimation of the spatial distribution $\bar{v}_z$, based on the measured spatial distributions of $\bar{v}_x$ and $\bar{v}_y$, was obtained. The computation of $\bar{v}_z$ was based on the time-averaged form of the continuity equation

$$\nabla \bar{v}^* = 0 \tag{4}$$

for which a first-order finite-difference approximation form is

$$\frac{\Delta \bar{v}_x}{\Delta x} + \frac{\Delta \bar{v}_y}{\Delta y} + \frac{\Delta \bar{v}_z}{\Delta z} = 0 \tag{5}$$

With the points from Grid 1, in experiments 1, 2, and 3 (see Table 2), the derivatives $(\partial/\partial x)\bar{v}_x(i, j, k)$ and $(\partial/\partial y)\bar{v}_y(i, j, k)$ were estimated from neighboring points using $\bar{v}_x(i - 1, j, k)$ and $\bar{v}_x(i + 1, j, k)$, for $\Delta\bar{v}_x/\Delta x$, $\bar{v}_y(i, j - 1, k)$ and $\bar{v}_y(i, j + 1, k)$ for $\Delta\bar{v}_y/\Delta y$. At the wall, the nonslip condition was always assumed. The numerical integration of $\bar{v}_z$ was made from the top. A simple corrective factor was computed at each plane, based on the difference of the calculated flow rate from the estimated $\bar{v}_z$ and the given flow rate, to avoid the accumulation of numerical errors throughout the mixing head. A complete description of the numerical integration to obtain $\bar{v}_z$ is presented in Teixeira.[26]

The results are summarized in Figure 5, where one can observe a clear back-mixing flow pattern resulting from a global time-averaged recirculation pattern between the injec-

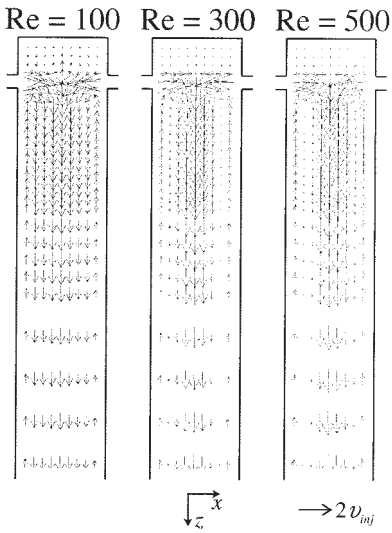

Figure 5. Vector maps for vertical velocity components at Re = 100, 300, and 500 on the vertical plane containing the injector's center.

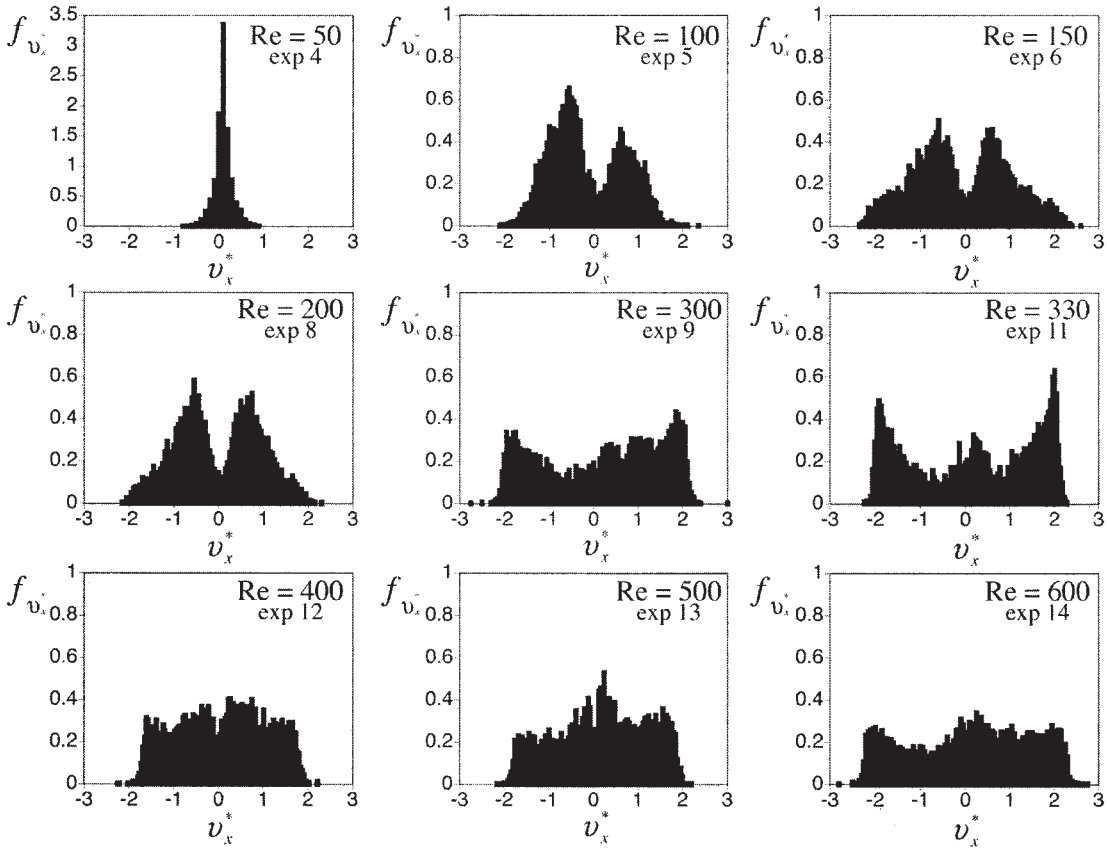

Figure 6. The pdf values of the horizontal velocity v_x^*, at the impingement point (0, 0, 5) for different values of Re.

tors and the exit. This important observation is consistent with the results presented in Figure 4, but it reveals only the main characteristic of the macromixing pattern inside the mixing head. To use the LDA data from the local mixing mechanisms, it was necessary to analyze the local characteristics of the velocities through the knowledge contained in the probability density functions of the horizontal velocities.

Probability density functions of v_x^*

The local probability density functions $f_{v_x^*}$ of the horizontal velocity component v_x^* can be calculated by

$$f_{v_x^*} = \frac{n_s\big|_{v_x^* \le v^* < v_x^* + \Delta v^*}}{n_t \Delta v_x^*} \tag{6}$$

where $n_s\big|_{v_x^* < v^* < v_x^* + \Delta v^*}$ is the number of samples in the velocity interval $[v_x^*; v_x^* + \Delta v_x^*]$, and n_t is the total number of samples. For each computed probability density function (pdf), at least 2000 velocity sample measurements were collected, and 120 velocity classes were used with a class width $\Delta v_x^* = (v_{x_{\max}}^* - v_{x_{\min}}^*)/120$, where $v_{x_{\max}}^*$ and $v_{x_{\min}}^*$ are the maximum and minimum dimensionless velocities, respectively, detected for each experiment.

The pdf values of v_x^* at the impingement point are shown in Figure 6, for increasing values of Re. At Re = 50, a laminar steady flow was obtained, and the pdf shows a unique mode centered at the zero lateral velocity, as expected, with some velocity symmetric spreading around zero stemming from the finite size of the LDA measuring volume (see Table 2). For Re = 100, a bimodal pdf is observed with the two modes centered around $v_x^* = \pm 1$. This result indicates the presence of some periodic oscillatory behavior, with an equal probability of finding either one of the jets originated on either side of the mixing head at the impingement point and, moreover, with a local average fluid horizontal velocity equal to the superficial velocities at the exits of the injectors. The same pattern is also observed for Re = 150 and Re = 200. For Re = 300, a different pattern is observed where the pdf values are no longer bimodal, showing a fairly uniform distribution between the maximum velocities, $v_x^* = \pm 2$. This indicates stronger dynamics and chaotic oscillations, with local velocities that can achieve the maximum velocity in the jet at the exit of the injectors. This can be interpreted as a loss of the identity of the jets at the impingement point for higher Re. These experiments clearly show that, when changing from Re = 50 to Re = 100, a *critical Reynolds number* for the transition from laminar to oscillatory flow must have been surpassed.

The spatial evolution of the pdf values at the centerline of the mixing head are analyzed in Figure 7. The first observation is that the jets' individual influence disappears at z = 10 mm, a very short distance from the injectors' position and equivalent only to half the diameter of the mixing head, a very clear indication that the turbulence levels are very high. The second observation is that the turbulence levels, measured by the spreading pdf values, fall very rapidly toward the exit.

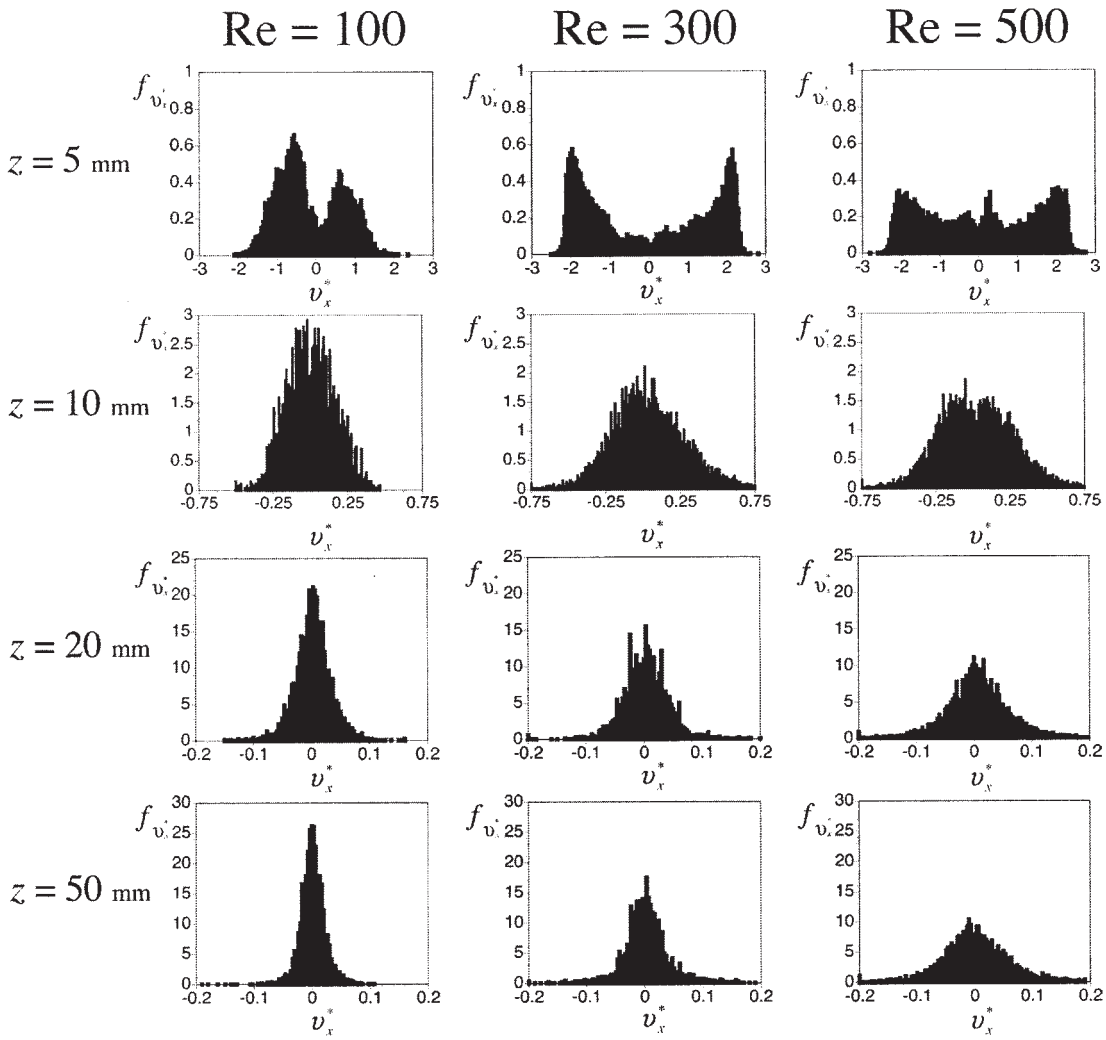

Figure 7. The pdf values of the horizontal velocity v_x^*, along the chamber axis: z = 5, 10, 20, and 50 mm for Re = 100, 300, and 500.

Turbulence intensity

The turbulence intensities (I_{v_x}) for each measurement location, computed as

$$I_{v_x} = \frac{1}{v_{inj}} \left\{ \frac{\sum_{i=1}^{n_t} [v_x(i) - \bar{v}_x]^2 t_{si}}{\sum_{i=1}^{n_t} t_{si}} \right\}^{1/2} \tag{7}$$

are shown in Figure 8, for some horizontal planes, z = 1, 3, 5, 10, and 50 mm at Re = 100, 300, and 500, as color maps obtained from the measurements with Grid 1. From these maps it is also observable—but now not only at the centerline—that the turbulence intensities are stronger at the top of the mixing head and peaking in front of the injectors, and decreasing strongly toward the exit. Furthermore, three new aspects can be clearly observed: (1) the turbulence intensities are always higher at the centerline; (2) the turbulence intensities increase with Re, as expected; and (3) the turbulence is clearly anisotropic in the regions near the injectors.

In an attempt to define a length scale l, where the jets from injectors are dominant, the average turbulent intensities in each plane, $I^*_{v_x}$, for all planes in Grid 1, are plotted in Figure 9. This figure clearly reveals within the range of Re studied, that high turbulence levels are mainly established in the top part of the mixing head over a length l, equivalent to 1.5 times its diameter.

Lee et al.[10] introduced the *number of mixing heads* parameter, $n = l/D$ and, based on their RIM photographic studies, proposed a value of $n = 3$, to be used in their mixing model to predict the mean striation thickness. Based on the striation thickness data of Kolodziej et al.,[2] Baldyga and Bourne[25] used $n = 2$ and $n = 3$ in their striation thickness distribution model, based on the statistical theory of turbulent diffusion, considering turbulence to be locally homogeneous and isotropic. Kusch et al.[13] also used the same parameter, with the lamellar model of Chella and Ottino,[27] to compare to their impingement mixing-reaction data, and used rather large values of n to attain a close match to the experimental results.

From the LDA data in Figure 9, it is now evident that n is smaller than the values previously obtained from photographic

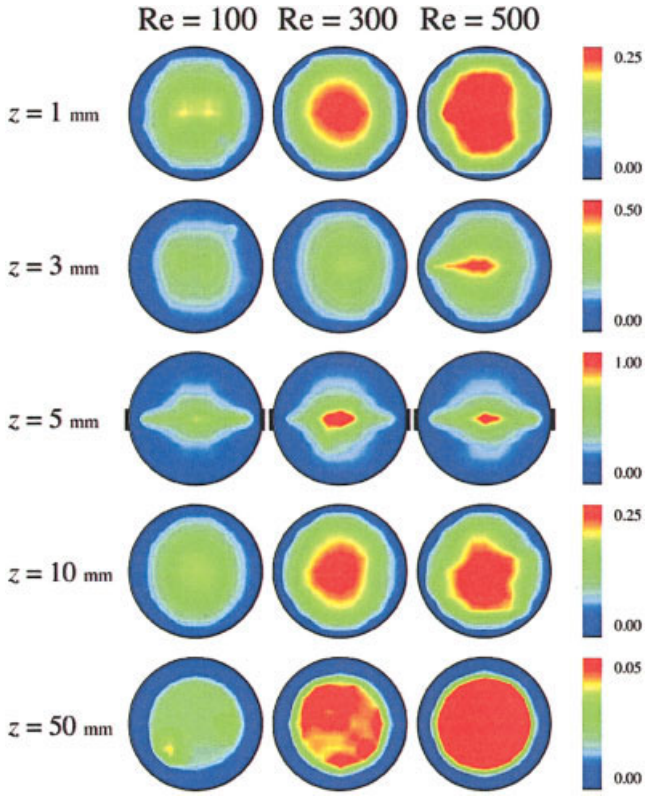

Figure 8. Maps of turbulence intensity $I^*_{v_x}$, for Re = 100, 200, and 300 at the horizontal planes, z = 1, 3, 5, 10, and 50 mm.

[Color figure can also be viewed in the online issue, which is available at www.interscience.wiley.com]

studies, and in this study acquires a value close to $n = 1.5$. Furthermore, this value is independent of Re within the typical operational range of RIM machines ($100 \leq \text{Re} \leq 500$).

To study the turbulence level and anisotropy dependency on Re, the ensemble average turbulence $\langle I^*_{v_x} \rangle$ and $\langle I^*_{v_y} \rangle$ were computed as the average of independent measurements of $I^*_{v_x}$ and $I^*_{v_y}$, respectively, at all locations for Grid 1 and Grid 2, and are plotted in Figure 10 as a function of Re. It is obvious that both turbulent levels increase critically above Re = 100, but are

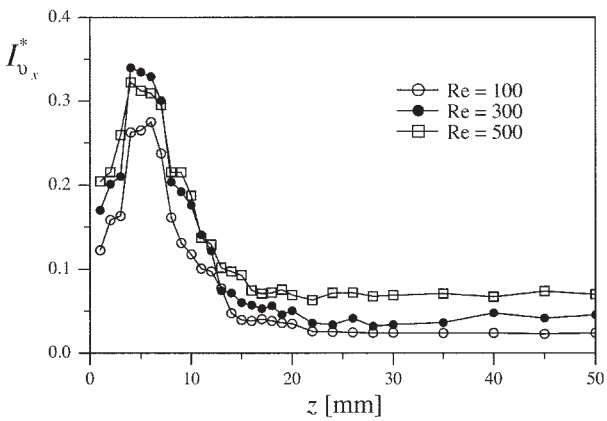

Figure 9. Evolution of turbulence intensity $I^*_{v_x}$, along the chamber axis for Re = 100, 200, and 300.

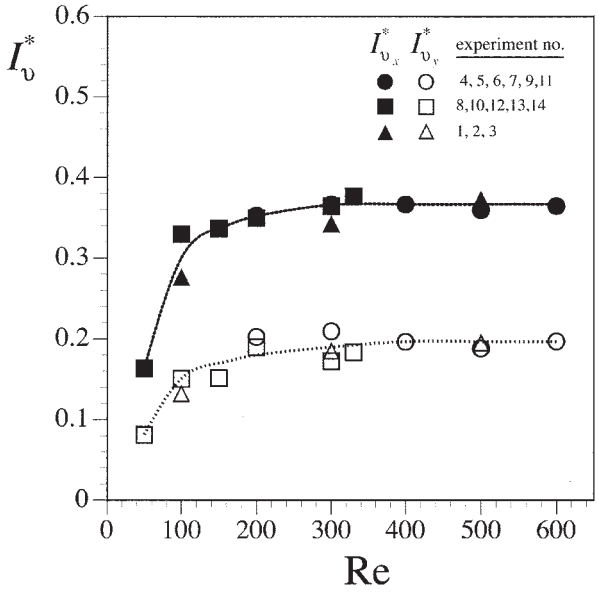

Figure 10. Evolution of turbulence intensity I^*_v with the Reynolds number.

practically constant, that is, independent of Re, for Re > 200. In addition, the anisotropy level, determined by the ratio $\langle I^*_{v_x} \rangle / \langle I^*_{v_y} \rangle$ is also constant, above the value of Re ≥ 200.

From Figure 10, where circles and squares stand for experiments with Sol. 1 and Sol. 2, respectively, the *similarity* of flow conditions is also obvious. For experiments using different fluids, but under the same Reynolds number, the values of $\langle I^*_{v_x} \rangle$ and $\langle I^*_{v_y} \rangle$ are closely matched. The pdf values of the velocity from experiments with the same Reynolds number, but using different fluids, also presented the same features. It can be thus concluded that the flow field features are determined from the Reynolds number regardless of the fluid viscosity, at least in the present range of viscosities.

Reynolds stresses

The local normalized Reynolds stresses values, τ^*_{xy}, defined as

$$\tau^*_{xy} = \frac{\overline{v'_x v'_y}}{v^2_{inj}} \tag{8}$$

where $\overline{v_x v_y}$ is the time-averaged product of v_x and v_y, the fluctuating velocity components, which were measured with the LDA system, accepting data only when a coincidence mode existed between each velocity measurement, at the locations of Grid 1.[26]

Figure 11 shows the maps of the experimentally measured τ^*_{xy} at the horizontal planes, z = 1, 3, 5, and 10 mm, for Re = 100, 300, and 500. Once again, it can be observed that the main turbulence is established in the top part of the mixing head in front of the injectors, and here the turbulence is strongly anisotropic and inhomogeneous. Moreover, the maps in Figure 11 for z = 1, 3, and 5 show that the scale of turbulence in this region is of the order of the mixing-head diameter.

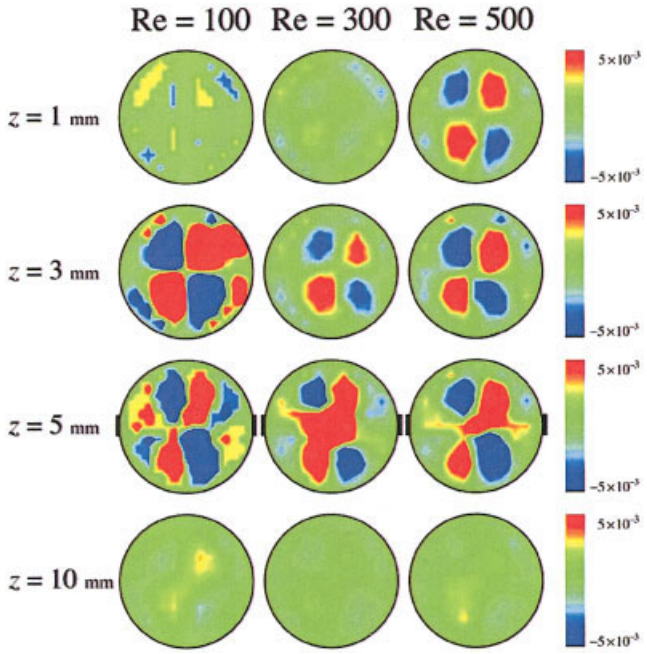

Figure 11. Maps of the Reynolds stresses for Re = 100, 200, and 300 at the horizontal planes, z = 1, 3, 5, and 10 mm.

[Color figure can also be viewed in the online issue, which is available at www.interscience.wiley.com]

Spectral analysis

It has already been hinted several times that the dynamics of the flow field are mainly oscillatory above a critical Re value, placed in the range 50–100. In addition, in several other previous studies on the mixing heads of RIM machines, the existence of a typical frequency has been observed for limited ranges of Re.[18-20] This frequency has been reported in dimensionless form as the Strouhal number, defined as

$$\mathrm{St} = \frac{fd}{v_{inj}} \tag{9}$$

where f is the frequency value of the flow characteristic oscillation.

Herein, the value of f was obtained from the frequency of the highest energy peak in the power-frequency spectra of the time series $v_x(t)$ obtained from LDA data. The slotted correlation technique, as proposed by Bell,[28,29] was used for the computation of the power-frequency spectra.[30]

Figure 12 shows the normalized power-frequency spectra G_{xx}, of $v_x(t)$, at the *impingement point* for increasing values of flow rates in the range of 250 $\geq$ Re $\geq$ 600. In this range—always above the critical Reynolds number—it could be detected that the jets tend to present typical oscillating frequencies at all times, based on the dominant peak of the spectrum, but other nonharmonic frequencies are also present with energies of the same order of magnitude as that of the dominant peak, pinpointing the chaotic characteristic of the flow.

Previous studies of Johnson and Wood[20] reported an upper limit of Re as only 150 for the detection of well-defined typical oscillation. Santos[30] observed that the typical oscillation frequency loses its associated well-defined energy peak with increasing Reynolds numbers because of the associated increase of turbulence levels as reported in this work. Figure 13 shows a summary of the measured Strouhal number values, based on the dominant peak frequency, as well as data reported in previous works.[19,20] It is clearly seen that in the range of Reynolds number of the present study the Strouhal number is maintained roughly constant, thus providing strong evidence that the same type of flow structures occur within the range of studied Re values.

Conclusions

A detailed experimental LDA characterization of the flow field in a RIM mixing head was reported, where local dynamical properties for mixing were revealed, and the spatial organization of the flow field determined, varying the flow rates and liquid viscosities within the typical operational Re range for RIM machines, 50 $\leq$ Re $\leq$ 600. From the measurements key features of the flow field were established for:

- The spatial distribution of mean velocities, turbulence intensity, and shear stresses.
- The pdf values of the velocity along the mixing chamber axis.
- The frequency characterization of the oscillatory behavior of the jets.
- The effect of the Reynolds number on the various flow features studied.

From the velocity pdf studies and the spatial average values of the turbulence intensity, the existence of two distinct flow regimes is apparent:

- At values of Re $\leq$ 50, the flow field is laminar and steady.
- In the range between Re = 50 and Re = 100, there must exist a critical Re value, for which occurs the flow-field transition from laminar to a *chaotic regime*. In this chaotic regime the velocities present bimodal pdf values, at the impingement point, and turbulence intensities are very high. Interactions of the jets constitute the main mixing mechanism around the impingement point.
- Above the critical Re, and for Re = 200, the turbulence intensities are roughly constant.

From LDA measurement spatial studies, it is also clearly revealed that:

- There is a *recirculation zone* consisting of a toroidal vortex upstream of the jets, and a *convection zone* with a back-mixing flow pattern downstream of the jets up to the mixing head exit.
- The spatial distribution of average velocities, turbulence intensities, and Reynolds stresses is roughly constant through Re = 100, 300, and 500, and showing consistently very strong gradients and anisotropic behavior.
- In the neighborhood of the jets' impingement point the flow-field dynamics is extreme, with the highest values of turbulence intensities and Reynolds stresses, within a top region of the mixing head of length equivalent to approximately 1.5 mixing-head diameters.
- Toward the outlet of the mixing head, the values of the intensity of turbulence are lower, but not negligible, and they increase steadily with increasing values of Reynolds numbers.

From the spectral analysis of LDA data, it is observed that the Strouhal number is roughly in keeping with Re, for 150 $\leq$

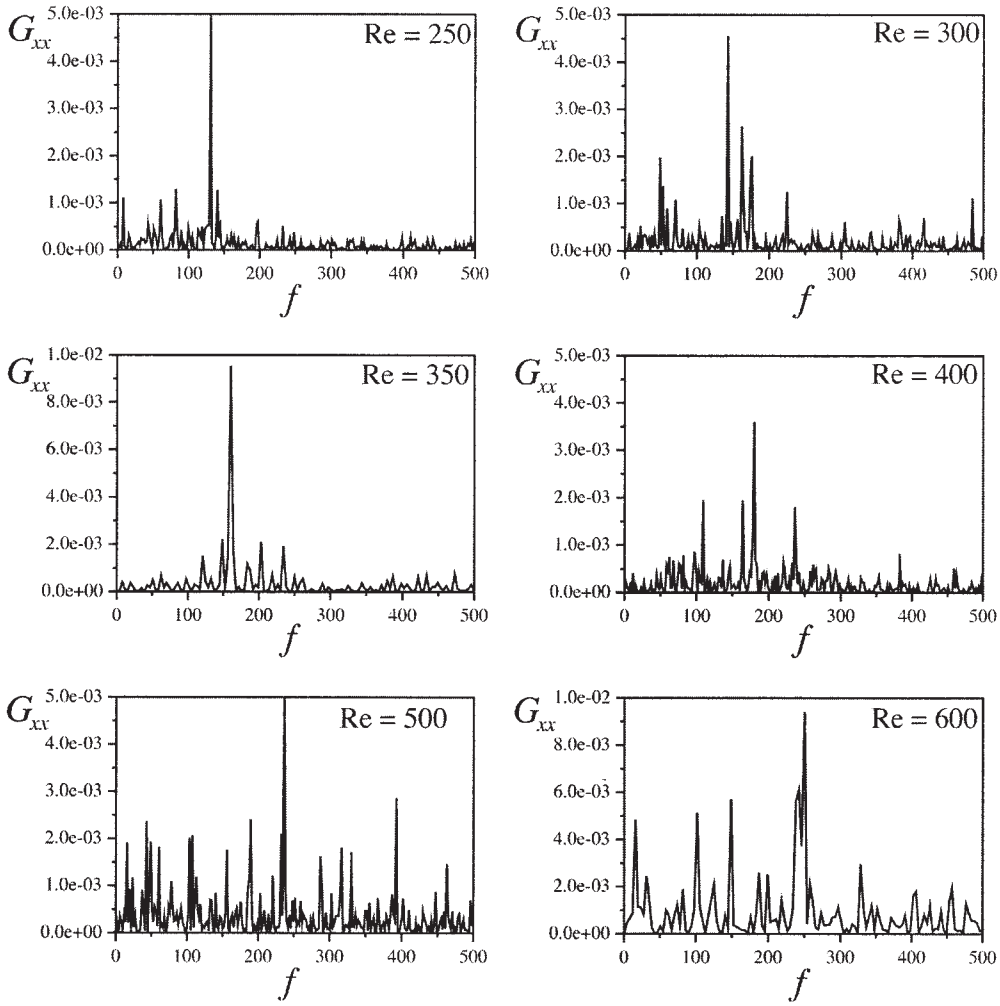

Figure 12. Power frequency spectra at the impingement point for Re = 250, 300, 400, 500, and 600.

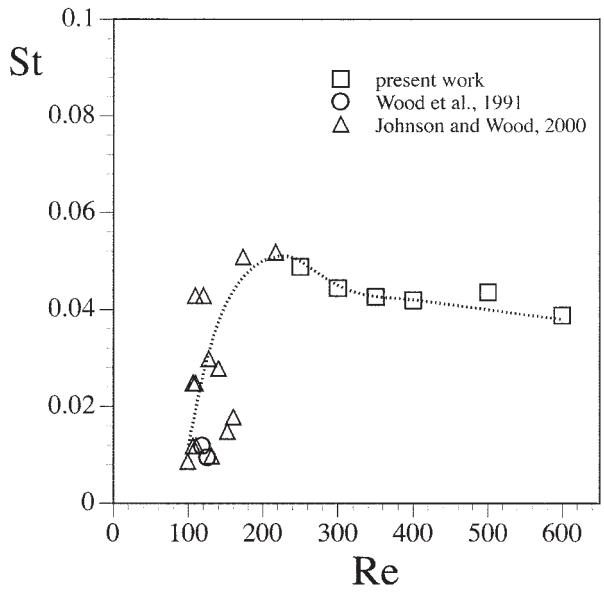

Figure 13. Plot of the Strouhal number vs. the Reynolds number, including other works in the literature.

Re ≤ 600, indicating the same type of dynamically evolving flow field structures in this range of Re.

The results obtained in this study represent a significant contribution to the knowledge of flow regimes and flow properties in the mixing heads of RIM machines in the transition of regimes from steady laminar to chaotic. The present characterization of the flow field with quantified properties will provide a sound basis for future experimental validations of new mixing models and the computational fluid dynamics simulations of RIM mixing hydrodynamics.

Acknowledgments

Financial support for this work was in part provided by the research programs FCT/PRAXIS/3/3.1/CEG/2565/95 and POCTI/34515/EQU/2000 for which the authors are thankful. André M. Teixeira and Ricardo J. Santos acknowledge their Ph.D. scholarships by FCT, PRAXIS XXI/BD/5475/95, and PRAXIS XXI/BD/17018/98, respectively.

Notation

d = diameter of injectors
D = mixing head diameter
f = frequency
$f_{v_x^*}$ = probability density function of v_x^*
G_{xx} = spectral energy

I_{v_x} = turbulence intensity
l = length of mixing in the mixing head
n = number of mixing head diameters where mixing occurs
n_s = number of samples in a velocity interval
n_t = total number of samples
q_{inj} = flow rate at each injector
Re = Reynolds number
St = Strouhal number
t = time
t_{si} = sample time interval
v = velocity
x, y, z = Cartesian space coordinates

Greek letters

μ = viscosity
ρ = density
τ_{xy} = Reynolds stresses

Subscripts

inj = at the injectors
x, y, z = x, y, or z component

Superscripts

$*$ = dimensionless
$'$ = fluctuating term
$\overline{\ }$ = average

Literature Cited

1. Oertel G. *Polyurethane Handbook*. Munich, Germany: Hanser; 1985.
2. Kolodziej P, Macosko CW, Ranz WE. The influence of impingement mixing on striation thickness distribution and properties in fast polyurethane polymerization. *Polym Eng Sci*. 1982;22:388-392.
3. Kolodziej P, Yang WP, Macosko CW, Wellinghoff ST. Impingement mixing and its effect on the microstructure of RIM polyurethanes. *Polym Eng Sci*. 1986;24:2359-2377.
4. Macosko CW. *RIM Fundamentals of Reaction Injection Molding*. Munich, Germany: Hanser; 1989.
5. Sebastian DH, Boukobbal S. Mixhead parameters governing impingement mixing effectiveness for polyurethane reactive injection molding processes. *Polym Process Eng*. 1986;4:53-70.
6. Coates PD. Optimal control of RIM mixing heads. *Plast Rubber Process Appl*. 1990;13:139-145.
7. Malguarnera SC, Suh NP. Liquid injection molding. I. An investigation of impingement mixing. *Polym Eng Sci*. 1977;17:111-115.
8. Tucker CL III, Suh NP. Mixing for reaction injection molding. I. Impingement mixing of liquids. *Polym Eng Sci*. 1980;20:875-886.
9. Unger DR, Muzzio FJ. Laser-induced fluorescence technique for the quantification of mixing in impinging jets. *AIChE J*. 1999;45:2477-2486.
10. Lee L, Ottino JM, Ran WE, Macosko CW. Impingement mixing in reaction injection molding. *Polym Eng Sci*. 1980;20:868-874.
11. Harris RF, Anderson RM, Shannon DM. Specialty polyurethane soft segments. II. Mixing studies in micro-RIM using polyether diamine oligomers containing backbone urea moieties. *J Appl Polym Sci*. 1992;46:1547-1560.
12. Tosun GA. A study of micromixing in tee mixers. *Ind Eng Chem Res*. 1987;26:1184-1193.
13. Kusch HA, Ottino JM, Shannon DM. Analysis of impingement mixing-reaction data: Use of a lamellar model to generate fluid mixing information. *Ind Eng Chem Res*. 1989;28:302-315.
14. Johnson BK, Prud'homme RK. Chemical processing and micromixing in confined impinging jets. *AIChE J*. 2003;49:2264-2282.
15. Nguyen LT, Suh NP. Effect of high Reynolds number on the degree of mixing in RIM processing. *Polym Process Eng*. 1985;3:37-56.
16. Johnson DA, Wood PE, Hrymak AN. The effect of geometrical parameters on the flow field of an opposed jet RIM mix head: Equal flow and matched fluids. *Can J Chem Eng*. 1996;74:40-48.
17. Khakhar DV. The behaviour of confined impinging jets. Proc. of International Conference on Recent Advances in Chemical Engineering; 1989:100-106.
18. Sandell DJ, Macosko CW, Ranz WE. Visualization technique for studying impingement mixing at representative Reynolds numbers. *Polym Process Eng*. 1985;3:57-70.
19. Wood PE, Hrymak A, Yeo R, Johnson DA, Tyagi A. Experimental and computational studies of the fluid mechanics in an opposed jet mixing head. *Phys Fluids A*. 1991;3:1362-1368.
20. Johnson DA, Wood PE. Self sustainable oscillations in opposed impinging jets in an enclosure. *Can J Chem Eng*. 2000;78:867-875.
21. Santos RJ, Teixeira AM, Costa MRPFN, Lopes JCB. Operational and design study of RIM machines. *Int Polym Process*. 2002;17:387-394.
22. Unger DR, Muzzio FJ, Brodkey RS. Experimental and numerical characterization of viscous flow and mixing in an impinging jet contactor. *Can J Chem Eng*. 1998;74:40-48.
23. Zhao Y, Brodkey RS. Averaged and time-resolved, full-field (three-dimensional), measurements of unsteady opposed jets. *Can J Chem Eng*. 1998;76:536-545.
24. Zhao Y, Brodkey RS. Particle paths in three-dimensional flow fields as a means of study: Opposing jet mixing system. *Powder Technol*. 1998;100:161-165.
25. Baldyga J, Bourne JR. Distribution of striation thickness from impingement mixers in reaction injection molding. *Polym Eng Sci*. 1983; 23:556-559.
26. Teixeira AM. *Flow in a RIM Machine Mixing Head*. PhD Dissertation. Porto, Portugal: Universidade do Porto; 2000.
27. Chella R, Ottino JM. Conversion and selectivity modifications due to mixing in unpremixed reactors. *Chem Eng Sci*. 1984;39:551-567.
28. Bell WA. Spectral analysis algorithms for the laser velocimetry: A comparative study. *AIAA J*. 1983;21:714-719.
29. Bell WA. Spectral analysis of laser velocimeter data with the slotted correlation method. Proc. of AIAA/ASME 4th Fluid Mechanics, Plasma Dynamics and Lasers Conf., Atlanta, GA; 1986.
30. Santos RJ. *Mixing Mechanism in Reaction Injection Moulding—RIM. An LDA/PIV Experimental Study and CFD Simulation*. PhD Dissertation. Porto, Portugal: Universidade do Porto; 2003.

Manuscript received Nov. 10, 2003, and revision received Oct. 19, 2004.